2023-07-01

Numerical investigation on the hydrodynamic performance of a 2D U-shaped Oscillating Water Column wave energy converter

Zhu, G

10.1016/j.energy.2023.127357
Energy
Elsevier BV

Energy 274 (2023) 127357

Contents lists available at ScienceDirect

Energy

journal homepage: www.elsevier.com/locate/energy

Numerical investigation on the hydrodynamic performance of a 2D U-shaped Oscillating Water Column wave energy converter

Guixun Zhu [a], John Samuel [a], Siming Zheng [a,b,*], Jason Hughes [a], David Simmonds [a], Deborah Greaves [a]

[a] School of Engineering, Computing and Mathematics, University of Plymouth, Drake Circus, Plymouth PL4 8AA, UK
[b] State Key Laboratory of Hydraulic Engineering Simulation and Safety, Tianjin University, Tianjin 300072, China

ARTICLE INFO

Keywords:
Oscillating Water Column
Geometric optimization
Efficiency
Wave load
Smoothed Particle Hydrodynamics

ABSTRACT

The U-Oscillating Water Column (U-OWC) is a wave energy harvester exploiting the working principle of oscillating water columns for capturing and converting energy from sea waves. U-OWC devices can be integrated into a breakwater to enable wave energy extraction and provide shelter for port activities. In this work, a coupled Smoothed Particle Hydrodynamics (SPH) model was developed and applied to investigate the hydrodynamics of a U-OWC breakwater. The numerical model is validated against the experimental results over a range of regular wave conditions. An extensive campaign of computational tests is then carried out, studying the effects of geometrical parameters on the hydrodynamic performance and wave loading over the U-OWC breakwater. It shows that the geometrical parameters of the U-shape have a significant effect on the air pressure inside the chamber and the load phase difference between the two sides of the lip wall. The minimum load and maximum capture efficiency designs for U-OWC breakwaters cannot be satisfied geometrically at the same time. This demonstrates that it is necessary to consider comprehensively the structural reliability and hydrodynamic performance in the design and construction of a U-OWC breakwater.

1. Introduction

In response to increasing energy demand and climate change, the development of clean and renewable energy sources is gaining more attention. A considerable portion of this additional renewable energy has already been generated from intermittent renewable sources such as wind and solar technology. Meanwhile, alternative kinds of sustainable renewable energy should also be developed to reach a broad energy mix. Wave energy is a high potential renewable energy source. Devices that convert wave energy into electricity are known as wave energy converters (WECs). Among the vast variety of WECs, the Oscillating Water Column (OWC) device is one of the most classical and has been widely studied [1]. A classic OWC device is composed of a water column and an air chamber above, with the bottom and sidewalls partly submerged and exposed to the sea. The water column is able to rise and fall in response to the incident waves. The trapped air is forced through a turbine to produce electricity.

Over recent decades, there has been much numerical research on OWC devices. It should be emphasized that most of the early simulations rely on potential theory, with the assumption of inviscid, irrotational, and linear flows. Evans [2] developed a theoretical model for OWC devices, in which the internal water surface was modelled as an imaginary stiff weightless rigid piston. The stiff piston model imposed force on the piston due to the pressure drop resulting from the power take-off (PTO) system. The stiff piston model may give good approximate results when the wavelength of incident waves is very long compared with the horizontal length of the air chamber. By assuming incompressible air, Evans [3] created a relationship between the diffraction characteristics and air pressure, and provided formulae for power measurement. To address air pressure, the uniform pressure distribution model, initially developed by Sarmento and Falcão [4], was employed on the free surface. The pressure distribution model applies air pressure uniformly to the uneven free surface. Evans and Porter [5] developed a potential flow theory model of an OWC, which is composed of a thin vertical surface-piercing barrier next to a vertical wall. They found that the changes in the draught of the vertical barrier led to changes in the frequencies where the maximum capture efficiency occurs. Ning et al. [6] developed a two-dimensional (2D) completely nonlinear wave tank using the higher-order boundary element method (HOBEM) to study on-shore OWC devices. The hydrodynamic efficiency of the device was found to be highly influenced by the incident wave amplitude for the given OWC geometrical parameters. Their model was

* Corresponding author at: School of Engineering, Computing and Mathematics, University of Plymouth, Drake Circus, Plymouth PL4 8AA, UK.
E-mail address: siming.zheng@plymouth.ac.uk (S. Zheng).

https://doi.org/10.1016/j.energy.2023.127357
Received 22 December 2022; Received in revised form 2 March 2023; Accepted 27 March 2023
Available online 30 March 2023

later extended by Wang et al. [7] to explore the nonlinear impacts and the viscosity influence on capture efficiency of a fixed OWC device.

Computational fluid dynamics (CFD) models are developed to solve the Navier–Stokes equations. Meshes or particles are used to accomplish spatial discretization of computation domains. CFD approaches offer the benefit of capturing all relevant hydrodynamic nonlinearities, in comparison to potential flow theory with lesser fidelity. The analysis of OWC devices under rough sea conditions is made possible by the high-resolution data that more computationally expensive CFD simulations provide. CFD models have been widely used to study OWC devices. El Marjani et al. [8] developed a numerical model for OWC devices using the commercial Fluent software. Energy losses encountered in the chamber are well predicted, and it was shown that their evolution follows a parabolic law with the frequency variation. Zhang et al. [9] used a two-phase level-set immersed boundary approach to investigate the effect of incident wave conditions and geometry of a fixed OWC device. It was found tat increasing the dimension of the orifice at the bottom of chamber leads to lower hydrodynamic efficiency of the OWC due to reduced pressure in the chamber. Luo et al. [10] studied a heave-only floating OWC device using the Fluent commercial software. Various wave conditions, damping factors and spring systems were simulated to optimize efficiency. The frequency band width of high efficiency can be adjusted by turbine damping coefficient and elasticity coefficient of mooring spring so as to harness more energy from marine environment with varied wave frequencies. Kamath et al. [11] investigated a 2D OWC under operational wave conditions using REEF3D, an open-source CFD package. The REEF3D solves the fluid flow problem using the incompressible Reynolds-averaged Navier–Stokes (RANS) equations along with the continuity equation. In addition to the wavelength of the incident waves, the wave steepness also has a significance impact on the hydrodynamic efficiency of an OWC device. Iturrioz et al. [12] used an OpenFOAM solver for wave and structural interaction to simulate an OWC in three dimensions. The model solves the three-dimensional (3D) RANS equations for two incompressible phases flows. Small-scale laboratory tests are carried out to verify the numerical findings. It was found that air compressibility is not relevant at the laboratory scale and was not taken into account in the numerical model validation process. However, air compressibility must be taken into account for realistic power production at the prototype scale. Vyzikas et al. [13] used an air–water two phase OpenFOAM solver based on RANS equations to explore the behaviour of a fixed OWC, and the numerical results were found to have an error of less than seven percent from the experiment. Furthermore, a decay analysis based on mechanical vibrations was presented to estimate the OWC resonance frequency. With the use of the OpenFOAM, Simonetti et al. [14,15] studied the effect of damping factor with the consideration of air compressibility, wall draught, and chamber length on power efficiency of an offshore stationary asymmetric OWC device within compressible/incompressible air phase. Deng et al. [16] used OpenFOAM to study the hydrodynamic performance of an offshore-stationary OWC device with a horizontal bottom plate. The results indicated that, particularly for long waves, a bottom plate with a small opening ratio and a moderately long bottom plate is beneficial for wave power extraction. López et al. [17] evaluated the influence of air compressibility on the performance of an OWC device through physical modelling. OpenFOAM tool based on RANS equations was used as a complementary tool to calibrate the pressure-vs-flowrate curves, enabling the flow rate to be determined based on the pressure drop measurements from the physical model. It was found that significant errors would be introduced in the assessment of wave power absorption should the air compressibility in the chamber be disregarded, and the errors were strongly influenced by the wave conditions and turbine-induced damping. Wang and Zhang [18] investigated an offshore dual-chamber OWC system, which is made up of two closely linked 3D circular sub-units that are aligned in the wave propagation direction using OpenFOAM. When resonant motion occurs in one chamber, in addition to the positive influences on itself, a contribution to the improvement of capture width ratio in another chamber can also be identified.

Noted that, most of the research has been focused on optimizing geometrical characteristics and power take-off (PTO) system to improve hydrodynamic performance. Improvements in optimizing energy extraction are one of the key milestones in consolidating the technology's progress towards the commercial stage. However, investigations of hydrodynamic forces on OWC devices have received more attention recently. Patterson et al. [19] proposed an early effort at the estimation of the force acting on an in-chamber back wall, but no supporting experiment was conducted. Boccotti [20] evaluated the wave forces on U-shaped OWC devices installed on caisson breakwaters. It was discovered that when the greatest force acted on the breakwater for a wave group, the air pressure inside the chamber was practically at its maximum. Small-scale experiments of 1:40 and 1:60 scales were used to assess the pressure on OWC caisson [21]. John Ashlin et al. [22] performed experiments to study the overall wave force on an OWC device. It was found that the total horizontal wave forces on the OWC device were greater than the vertical wave forces. The effects of geometry on wave force of fixed OWC devices were studied experimentally and numerically by Ning et al. [23]. It was found that the horizontal wave force became larger when the length of the wave decreased. Konispoliatis et al. [24] studied wave forces on a three-OWC array. Viviano et al. [25] studied the wave forces of OWC devices under random waves. On an offshore OWC device, Elhanafi [26] used Star-CCM+ to forecast the wave loads acting on an offshore OWC device. The largest heave force was observed when the incident wave period reached natural frequency. Elhanafi et al. [27] also used experiments and a numerical model to study the impact of sidewalls on the OWC device's wave loads. Viviano et al. [28] further investigated the wave force with different scales. On an OWC-pile device, Huang et al. [29] ran a 3D numerical simulation and found that the wave forces and bending moment rose with wave height. Pawitan et al. [30] developed a model based on large-scale experiments to predict the wave forces. The vertical force was discovered to have a considerable impact on the overturning and sliding of OWC devices. Under regular waves, Viviano et al. [31] studied the wave forces on both sides of the front wall. Wang and Ning [32] then conducted a comprehensive analysis of the viscosity effects on the wave force. Wang et al. [33] examined wave forces on a dual-chamber OWC apparatus that was attached to the ground. Zhou et al. [34] developed a second-order HOBEM to predict wave forces on a stationary cylindrical-type OWC device.

To prevent the structure from slipping or overturning, an OWC caisson designer should design the structure for the expected maximum loads. Load evaluation is essential for design of operability and reliability. In 1985, a 500 kW demonstration plant based on a multi-resonant OWC system was built at Toftestallen, Norway [35]. A severe winter storm partially destroyed the plant after four years of operation. Bolts connecting the steel structure to the concrete structure were vulnerable to fatigue fracture [35]. A 16-chamber OWC breakwater at Mutriku is another example. Storms in 2007 and 2008, as well as 2009, caused significant damage. These incidents highlight the need for more investigation into overall structure loads [36]. The design of the OWC thus needs to consider not just its hydrodynamic efficiency but also the hydrodynamic loads. The interaction between waves and the OWC structure is particularly nonlinear under stormy sea conditions. Incident waves hitting the front wall can cause wave breaking and large slam loads. In the event of extreme sea conditions, the chamber may even experience violent sloshing. These nonlinearities show that it is not easy to study OWC installations under rough sea conditions.

Smoothed Particle Hydrodynamics (SPH) is one of the most well known mesh-free techniques and is often used in the research of complicated free-surface flows. The fluid domain is discretized into a set of particles based on kernel interpolation in the SPH framework. As a Lagrangian method, SPH works with discrete particles and determines each particle's motion independently. The SPH approach

captures the free-surface without the need of an algorithm to identify and follow the free-surface. It is regarded as a flexible approach that can easily handle severe deformations, unstable and nonlinear flows, and complicated topological evolution. The SPH model is therefore well suited to simulate the hydrodynamics of OWC installations under rough sea conditions. More recently, SPH methods have started to be used in OWC studies. Using SPHyCE, Didier et al. [37] studied an onshore OWC device by comparing results with data from FLUENT. The numerical results demonstrated that the SPH model could simulate the interaction of wave OWC structures under severe sea conditions well. Crespo et al. [38] used DualSPHysics to simulate an offshore OWC device with a mooring system. The parallel computing power of GPUs was also exploited, with which real complex geometries and domains could be simulated at a reasonable computational time. Wen et al. [39] considered turbulence effects in the SPH model to simulate an onshore OWC device. Sloshing conditions were found when the OWC device has a short front wall. Although the above studies showed that the SPH model could simulate the wave–structure interactions of OWC devices well, neither of them considered the air pressure inside the OWC chamber, not to say the assessment of wave power absorption. To solve that, Zhu et al. [40] proposed a single-phase SPH model with the consideration of the effect of a uniform air pressure distribution over the free surface inside the OWC chamber to assess the performance of OWC devices. Without needing to model the air phase, the air pressure is computed using a parabolic expression between pressure and airflow rate. An alternative is to represent the PTO system of the OWC by a plate inside the chamber, e.g., see Quartier et al. [41] who employed the project Chrono multi-physics package to impose forces on the plate to consider the effect of air pressure. The plate method is expected to give good approximate results for low wave frequencies. Both of these models implement the simulation of a PTO system in a single-phase model.

In the present study, the effects of the geometrical parameters on the hydrodynamic performance and wave loads of a U-OWC breakwater are investigated using SPH method. The U-shaped OWC device is a variant OWC device proposed by Boccotti [42], which adds a bottom-mounted vertical barrier in front of a conventional OWC device. In comparison with a typical OWC device, the vertical duct dramatically alters the excitation shape of the U-OWC device. Adjusting the geometry of the U-pipe allows the natural frequency of the U-OWC to be adjusted over a wide range [43]. Thus, U-OWC devices can achieve high capture efficiency over a wide range of periods. Another advantage is that sand and stones are prevented from entering the interior of the chamber due to the external submerged wall [44]. Boccotti [43] proposed a theoretical framework for U-OWC devices based on the unstable Bernoulli theorem and conducted experiments to verify the theoretical model [45]. Boccotti [20] tested various engineering requirements for a full-size U-OWC device. Arena et al. [46] outline the key difficulties surrounding the design and fabrication of the U-OWC devices. Malara and Arena [47] proposed a numerical model employing linear potential theory for the flow field outside the chamber of U-OWC devices and further enhanced the model with the consideration of head losses. Malara and Arena [48] studied the efficiency of a multi-U-OWC system. Multi-U-OWC systems were less efficient than single U-OWC systems. However, this problem could be effectively solved by adjusting the distance between U-OWCs. Vyzikas et al. [13] conducted experiments of various OWC devices. U-OWC devices with a sloping bottom in front of the submerged wall could achieve higher efficiency at the natural frequency. Scialò et al. [49] investigated the choice of the PTO system of U-OWC systems with multi-connecting chambers. A nonlinear model was developed by Scandura et al. [50] to simulate U-OWC devices, and the numerical results showed good agreement with experimental data with/without the top cover. This is in addition to a number of U-OWC related studies [51–54]. U-OWC devices on shore can be integrated into breakwaters. This combination reduces the construction and maintenance costs. At the same time, OWC devices can reduce wave reflection enhancing the hydraulic performance of the breakwater. For U-OWC type breakwaters, it is necessary to consider both the reliability of the structure when seeking to maximize energy extraction. The study focuses on both the optimum capture efficiency design and the minimum wave load design. The main objective is to take a comprehensive view of capture factor and wave loads to determine the U-shaped geometry design. This is achieved through laboratory experiments and comparison with a coupled single-phase SPH with a pneumatic model. The model is described in Section 2. Section 3 describes the experimental and numerical setup. Validations of the present model are described in Section 4. Section 5 gives the analysis of the geometrical effects on the hydrodynamic performance and wave loads. Finally, conclusions are drawn in Section 6.

2. Coupled SPH model

SPH is a highly advantageous method for simulating such strongly nonlinear sea conditions when extreme waves slam against OWC devices. Nevertheless, one of the drawbacks of the SPH method is its low computational efficiency. Each particle should be interpolated with tens or even hundreds of neighbouring particles. The number of neighbouring particles in SPH is far greater than the number of neighbouring nodes for mesh methods (finite volume method (FVM), finite element method (FEM), and so on). Secondly, modelling incompressible fluids requires a small time step (weakly compressible SPH model). Therefore, the calculation cost of the SPH model is much higher than that of the grid-based method. Although the current problem is two-dimensional, SPH still requires large computational cost.

In comparison, OceanWave3D is a potential flow theory-based model and provides efficient simulation of surface waves and velocity fields with satisfactory results. Therefore, a two-way coupled model between SPH and OceanWave3D is used here. In the flow region near OWC devices, the expensive SPH model is used to capture the nonlinear conditions. While the other region can be solved using the efficient OceanWave3D model to reduce the computational cost. This coupled model can improve the computational efficiency of the numerical model without compromising the ability of the SPH model in dealing with nonlinear problems.

2.1. SPH model

Here, the interest is in using SPH model to simulate incompressible free-surface flows in the field of ocean engineering, where the characteristic Mach numbers are very moderate and compressibility effects are small. In light of this, it is reasonable to assume a barotropic fluid, i.e. a fluid for which the pressure is a function of the density only and changes in the internal energy can thus be neglected. The continuity and Navier–Stokes equations in Lagrangian form for a weakly-compressible fluid are:

$$\begin{cases} \frac{\mathrm{d}\rho}{\mathrm{d}t} = -\rho\nabla\cdot\mathbf{u}, \\ \frac{\mathrm{d}\mathbf{u}}{\mathrm{d}t} = -\frac{1}{\rho}\nabla p + \nu\nabla^2\mathbf{u} + \mathbf{g}, \end{cases} \tag{1}$$

where ρ, $\mathbf{u}$, t, ν and p denote density, velocity vector, time, kinematic viscosity and pressure, respectively. $\mathbf{g}$ represents the gravitational acceleration.

The governing equation can be discretized by a δ-SPH approximation [55–57]. The δ-SPH formulation can be written as:

$$\begin{cases} \frac{\mathrm{d}\rho_i}{\mathrm{d}t} = -\rho_i \sum_j (\boldsymbol{u}_j - \boldsymbol{u}_i)\cdot\nabla_i W_{ij} V_j + \delta hc \sum_j \boldsymbol{\Psi}_{ij}\cdot\nabla_i W_{ij} V_j, \\ \frac{\mathrm{d}\boldsymbol{u}_i}{\mathrm{d}t} = -\frac{1}{\rho_i}\sum_j (p_j + p_i)\cdot\nabla_i W_{ij} V_j + \alpha hc \sum_j \boldsymbol{\Pi}_{ij}\nabla_i W_{ij} V_j + \boldsymbol{g}, \end{cases} \tag{2}$$

where W_{ij} is the kernel function, c is numerical sound speed. If not specifically stated, δ and α are 0.1 and 0.01, respectively. The density diffusion is added in the continuity equation to avoid spurious numerical oscillations. The Ψ_{ij} in density diffusion is written as:

$$\begin{cases} \Psi_{ij} = & 2(\rho_j - \rho_i)\frac{\mathbf{r}_j - \mathbf{r}_i}{|\mathbf{r}_j - \mathbf{r}_i|^2} - (\langle\nabla\rho\rangle_i^L + \langle\nabla\rho\rangle_j^L), \\ \langle\nabla\rho\rangle_i^L = & \sum_j (\rho_j - \rho_i)\mathbf{L}_i\nabla_i W_{ij}V_j, \\ & \text{where } \mathbf{L}_i = \left[\sum_j (\mathbf{r}_j - \mathbf{r}_i)\otimes\nabla_i W_{ij}V_j\right]^{-1} \end{cases} \tag{3}$$

where $\otimes$ denotes tensor product. The Π_{ij} in the viscosity term is given as:

$$\Pi_{ij} = \frac{(\mathbf{u}_j - \mathbf{u}_i)\cdot(\mathbf{r}_j - \mathbf{r}_i)}{|\mathbf{r}_j - \mathbf{r}_i|^2}. \tag{4}$$

For OWC devices, water and air are strongly coupled inside the OWC chambers. The air pressure in the OWC chamber acts on the free internal water surface and affects the oscillation of the water column directly. In order to consider a pneumatic model in a single-phase SPH model, the air pressure P_a is added into the pressure gradient [40,58]. The discrete pressure gradient inside the chamber is rewritten as:

$$-\frac{1}{\rho_i}\nabla p_i = -\frac{1}{\rho_i}\sum_j [(p_j + p_a) + (p_i + p_a)]\cdot\nabla_i W_{ij}V_j. \tag{5}$$

To represent the connection between air velocity and air pressure inside the chamber, the quadratic formulas are utilized:

$$p_a = K_{dm}|q_d|q_d, \tag{6}$$

where K_{dm} is the damping coefficient and q_d is the air flow velocity per unit at the orifice. $q_d(t) > 0$ denotes that air flows into the chamber.

Meanwhile, the fluid pressure is related to the density explicitly according to the concept of artificial compressibility. Then, the pressure is obtained through the equation of state as:

$$p = (\rho - \rho_0)c^2, \tag{7}$$

where ρ_0 is the initial particle density. In the present simulation, a prediction–correction time-stepping scheme is applied to ensure second-order accuracy [59]. While the front wall of the U-OWC devices is simulated by the regional ghost particle approach [40]. Following [56,60], the present model uses the regular fixed ghost particles that are created to represent the other solid boundaries.

2.2. OceanWave3D

OceanWave3D was proposed by Bingham and Zhang [61],Engsig-Karup et al. [62] for large-scale modelling of wave problems in coastal and offshore environments, based on a fully nonlinear potential flow theory. OceanWave3D numerically solves the potential flow governing equations [63] for gravity waves at the water surface in a 3D Eulerian reference system using a right-angle coordinate system (x, y, z). The problem of non-breaking free surface waves can be described in terms of the velocity potential energy ϕ and the z position η of the free surface. At a free surface, nodes should remain at the surface with a pressure equal to the atmospheric pressure. At the bottom, the no penetration condition is set. The kinematic and dynamic boundary conditions of the free surface, and bottom boundary condition are:

$$\frac{\partial\eta}{\partial t} = -\frac{\partial\eta}{\partial x}\frac{\partial\tilde{\phi}}{\partial x} - \frac{\partial\eta}{\partial y}\frac{\partial\tilde{\phi}}{\partial y} + \tilde{w}\left[1 + \left(\frac{\partial\eta}{\partial x}\right)^2 + \left(\frac{\partial\eta}{\partial y}\right)^2\right], \tag{8}$$

$$\frac{\partial\tilde{\phi}}{\partial t} = -\frac{1}{2}\left[(\frac{\partial\tilde{\phi}}{\partial x})^2 + (\frac{\partial\tilde{\phi}}{\partial y})^2\right] + \frac{1}{2}\tilde{w}^2\left[1 + (\frac{\partial\eta}{\partial x})^2 + (\frac{\partial\eta}{\partial y})^2\right] - g\eta, \tag{9}$$

$$\frac{\partial\phi}{\partial z} + \frac{\partial h_o}{\partial x}\frac{\partial\phi}{\partial x} + \frac{\partial h_o}{\partial y}\frac{\partial\phi}{\partial y} = 0, \quad z = -h_o, \tag{10}$$

where $h_o = h_o(\mathbf{x})$ is the water depth from the seabed to the still water level. $\tilde{\phi} = \phi(\mathbf{x}, \eta, t)$ is the velocity potential of the free surface, $\mathbf{x} = (x, y)$ represents the horizontal position and $\tilde{w}$ is the vertical velocity of the free surface.

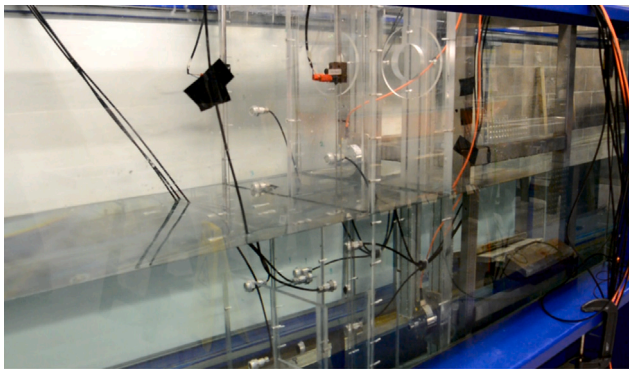

Fig. 1. Photograph of the COAST laboratory wave flume and U-OWC model.

The σ coordinate transformation allows a fixed grid distribution to be obtained taking into account free surface variations:

$$\sigma = \frac{z + h_o(\mathbf{x})}{\eta(\mathbf{x}, t) + h_o(\mathbf{x})}. \tag{11}$$

The time integration method uses the classical fourth-order Runge–Kutta method. Wave generation and absorption is achieved using the relaxation zone method proposed by Larsen and Dancy [64].

2.3. Coupling strategy

To combine the SPH model and OceanWave3D, an open relaxation boundary in SPH model is developed. The open relaxation boundaries are implemented as open and relaxation zones. Relaxation zones are implemented to establish the smooth continuum of horizontal velocity and free surface elevation in the relaxation region from the OceanWave3D to the SPH results. Horizontal velocity and free surface level from OceanWave3D is imposed on these relaxation particles. A relaxation function is applied here, which is an extension to that of Mayer et al. [65] and has been used in [66]. The relaxation function is:

$$\alpha_r(i) = 1.0 - \frac{\exp(\chi_{rs}^{\beta}) - 1}{\exp(1) - 1}, \quad i \in R1, \tag{12}$$

where $\beta = 3.5$ is relaxation coefficient, $\chi_{rs} = \frac{|x_i - x_{r1}|}{L_r}$. x_{r1} are the horizontal positions of the interfaces between the relaxation zones and the fluid zone. x_i is the position of particle i. $R1$ denotes the coupling region. L_r is the length of the coupling region. Then the horizontal velocity $\boldsymbol{u}_x$ and free surface level η is modified in the following way:

$$\boldsymbol{\Phi}_a = \alpha_r(\boldsymbol{\Phi})_a^{SPH} + (1 - \alpha_r)(\boldsymbol{\Phi})_a^{OceanWave3D}. \tag{13}$$

where $\boldsymbol{\Phi}_a$ denote horizontal velocity and free surface level. Once the corrected free surface level η_i is obtained, η_i is imposed on relaxation particles. In the relaxation zone, the fluid particles near the free surface are generated or removed in reference to the corrected free surface level η_i.

The main purpose of the open zone is to avoid the effects of kernel truncation. The horizontal velocity and free surface level from OceanWave3D at the open zone are imposed. To obtain the vertical velocity and density of the open particles, a moving least-squares reconstruction is used.

In OceanWave3D, only free surface quantities can be coupled. Thus, the coupling is limited to the surface elevation ϕ and the vertical free surface velocity $\tilde{w}$. In the present coupled model, the free surface elevation and vertical free surface velocity inside the open relaxation boundary are transferred. To ensure a smooth transition from SPH results to OceanWave3D data, the same relaxation function as the one in the SPH model is used. When coupling the two models, the coupling strategies under a parallel system is achieved. The parallel framework regarding SPH can be found in Zhu et al. [67]. A detailed description of the coupling strategy can be found in Zhu [68].

Table 1
Wave parameters for investigating related hydrodynamic performance.

Case	Wave period (s)	Wave height (m)	Wave length (m)	Wave steepness
1	2.15	0.050	4.96	0.010
2	2.15	0.100	4.96	0.020
3	2.15	0.150	4.96	0.030
4	2.15	0.247	4.96	0.050
5	1.96	0.100	4.42	0.052
6	1.70	0.100	3.67	0.027

2.4. Hydrodynamic efficiency of U-OWC

The capture efficiency C_w of an OWC device can be obtained by comparing the energy of the incident wave (P_{inc}) with the energy absorbed by the OWC devices (P_{owc})

$$C_w = \frac{P_{owc}}{P_{inc}}. \tag{14}$$

In laboratory experiments, the energy absorbed by the OWC devices can be obtained from the air flow at the opening versus the air pressure

$$P_{owc} = \frac{1}{T}\int_{t_0}^{t_0+T} Q_t p_a \mathrm{d}t, \tag{15}$$

where t_0 is a time after the system has reached a steady state. Q_t is the air volume per second going through the orifice ($Q_t = Al q_d$). $Al = \pi r_o^2$ is the sectional area of the orifice (r_o denotes the radius of the orifice).

According to linear wave theory, the incident wave power can be calculated as [9]:

$$P_{inc} = \frac{1}{4}\rho g A_i^2 \frac{\omega}{k_w}\left(1 + \frac{2k_w d}{\sinh(2k_w d)}\right), \tag{16}$$

where A_i is the incident wave amplitude, k_w is wave number.

3. Experimental and numerical setups

The experiments of a small-scale U-OWC breakwater were carried out at the University of Plymouth to validate the numerical model. The wave flume is 35 m long with a water depth 0.675 m. An U-OWC breakwater was placed before the end of the flume with the back wall of the structure at a distance of 27.0 m from the wave paddle. Fig. 1 shows a photograph including the laboratory wave tank and the physical model of the U-OWC breakwater. An orifice is used to simulate the damping of the turbine. The orifice radii used in the tests was 4 mm. This corresponds to an opening ratio O_r of 0.7%, which represents the ratio of the top opening to the area of the entire top cover. Eight pressure sensors were placed on the lip wall facing outside (P1–P6) and inside the chamber (P7 and P8), as shown in Fig. 2. P5, P7, and P8 have the same vertical position. Four wave heights and three periods were considered, as shown in Table 1. The bottom and side clearances of the U-OWC WEC were designed to avoid the transfer of wave loads to the flume walls and bottom. This allows two load cells, which are placed at the back of the device provided to accurately measure the true wave loads on the system yet this is out of the scope of the present study.

The numerical simulations have the same setups (including location of measurement points) as the experiment. The numerical wave flume is shown in Fig. 3. The entire computational domain is divided into two parts: the SPH region and the OceanWave3D region. The SPH region is used to simulate areas around the OWC where wave slamming, wave breaking and other nonlinear phenomena may occur. Thus, numerical regions from 18 m to 27 m are simulated using SPH. 18 m is the beginning of the coupling region, and the length of the overlapping region is half the incident wave wavelength. Therefore, the length of the coupling region varies for different incident waves. Fig. 3 shows 49 sub-domain divisions using 49 cores. 1 core is used for the OceanWave3D solver, whereas the remaining 48 cores are used for the SPH solver. First, the validation was carried out by comparing the data from both physical and numerical models. Once the numerical model was validated, the model was used to analyse the effect of the geometry on the wave loads of the U-OWC breakwater. Then, different geometrical designs of the U-OWC breakwater were modelled. The influences of the width and height of the U-shaped structure on the wave loading were considered. Studies in this paper were conducted on the Fotcluster2 in High Performance Computer Centre in the University of Plymouth. Fotcluster2 is a 752 core distributed-memory cluster, which is comprised of: a 3U combined head ς storage node, plus 56 compute nodes. The tests were conducted on the phase2 consisting of 36 Viglen $HX425T^2i$ HPC 2U Compute Nodes, equipped with Dual Intel Xeon E5650 (Westmere) Six Core 2.66 GHz processors and 12 GB of memory per motherboard.

4. Model validation

4.1. Damping factor

For an impulse turbine, the air pressure drop across the turbine is approximately proportional to the air flow rate squared. Similar quadratic relationships between the air pressure and air flow rate can be reproduced by an orifice plate. Indeed, the orifice plate has been widely adopted to simulate an impulse turbine in the physical tests of the OWC device (e.g., see [14,69–71]). The damping effect of the orifice can be adjusted by changing the diameter of the orifice. The smaller the size of the orifice, the larger the damping coefficient. For the orifice with a radius of 4 mm, the damping coefficient K_{dm} is 1.47, which is determined by fitting a quadratic curve with the measured data of air pressure and flow rate (see Fig. 4). The damping factor is used to obtain the instantaneous air pressure from the flow rate/pressure relationship in Eq. (6) in the pneumatic model. The velocity ΔV_f of the free surface is calculated using the following equation,

$$\Delta V_f = \frac{\eta_{n+1} - \eta_n}{t_{n+1} - t_n}, \tag{17}$$

where η_n and t_n denote the free surface level and the time, respectively, at the n time points. One can obtain the air flow velocity per unit q_d at the orifice

$$q_d = \frac{\Delta V_f}{O_r}. \tag{18}$$

The relationship between the air flow velocity per unit and the air pressure inside the chamber is shown in Fig. 4. $K_{dm} = 1.47$ is obtained by fitting Eq. (6) to the physical data set for opening ratio O_r of 0.7% with a satisfactory correlation coefficient ($R^2 = 0.932$).

4.2. Convergence test

In SPH region, the fluid domain is discretized by a set of fluid particles. These fluid particles are free to move and carry physical information, such as mass, density, pressure, and velocity. The solid boundary in SPH region is discretized by a set of fixed ghost particles. In OceanWave3D region, the computational domain is discretized by a grid of uniformly distributed nodes along the horizontal direction. Due to the σ coordinate transformation, the nodes are always fixed. In the σ transformed domain, several nodes are defined in the vertical direction below each horizontal free-surface grid point, in the restricted range $0 \le \sigma \le 1$.

In the beginning, the computational domain in SPH region is discretized by regularly distributed particles. Therefore, the discrete strategy is concerned with the initial particle spacing. In OceanWave3D, discretization strategy is implemented by adjusting the number of grid nodes in the horizontal and vertical directions, for a given size of the domain, to refine or coarsen the spatial resolution. Therefore, the discrete strategy of the SPH region and OceanWave3D both should be considered when conducting convergence test.

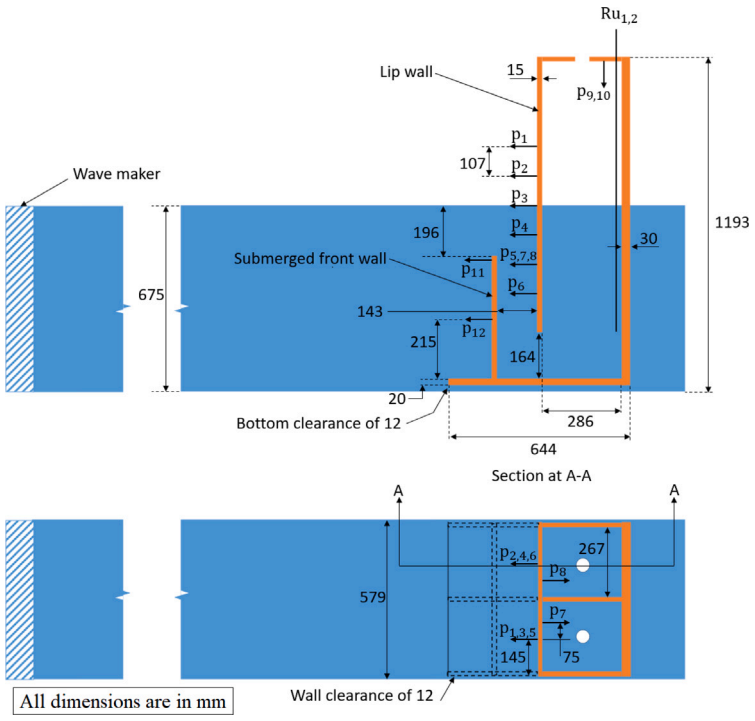

Fig. 2. Side elevation and plan views of the U-OWC model in the wave flume.

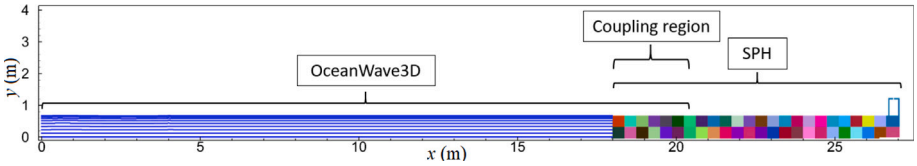

Fig. 3. Sketch of subdomain distribution in the numerical wave tank.

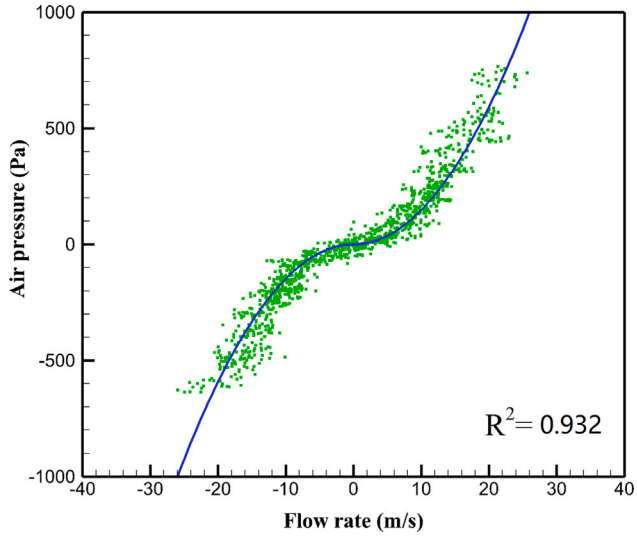

Fig. 4. Air pressure p_a versus air flow velocity per unit q_d for the orifice with a radius of 4 mm (opening ratio O_r of 0.7%). Green dots: experimental data; Blue line: fitting curve by using Eq. (6) with $K_{dm} = 1.47$.

Numerical tests were performed to assess the convergence of the adaptive spatial and temporal discretization for case 4. Three mesh numbers ($x \times y$): 1000 × 10, 2000 × 10 and 4000 × 10, and three initial particle spacing: 0.02 m, 0.01 m, 0.005 m are selected, as shown in Table 2. For quantifying and better evaluating the comparison between the reference results, the mean average errors for amplitude MAE_a1 and phase MAE_p1 are used, which are calculated according to equations

$$MAE_a1 = \frac{1}{N_a}\sum \frac{|\eta_{extr}^{ref} - \eta_{extr}^{sph}|}{2.0 * |\eta_{extr}^{ref}|}, \tag{19}$$

$$MAE_p1 = \frac{1}{N_a}\sum \frac{|t_{extr}^{ref} - t_{extr}^{sph}|}{T_4}, \tag{20}$$

where $extr$ refers to the local peak values, T_4 to the wave period of case 4 and $N_a = 6$ to the number of wave crest in Fig. 5. ref and sph denote reference data (Case C1) and SPH results, respectively.

Fig. 5 depicts the time history of the free surface elevation at the position of Ru_1 (see Fig. 2). The results obtained using the C1, C2 and C3 meshes are identical, indicating that mesh convergence was achieved using mesh number 1000 × 10. As the initial particle spacing decreases, the error between the numerical results decreases gradually. Balancing the calculation cost with convergence, the initial particle spacing of 0.01 m was used. Finally, the mesh number 1000 × 10 and initial particle spacing 0.01 m are selected for the following research.

4.3. Validation

Fig. 6 shows the time histories of free surface and air pressure inside the chamber for wave case 2. The predicted phases of the wave surface elevation agree well with the experimental data, although there are slight deviations in their amplitudes. The air pressure from the

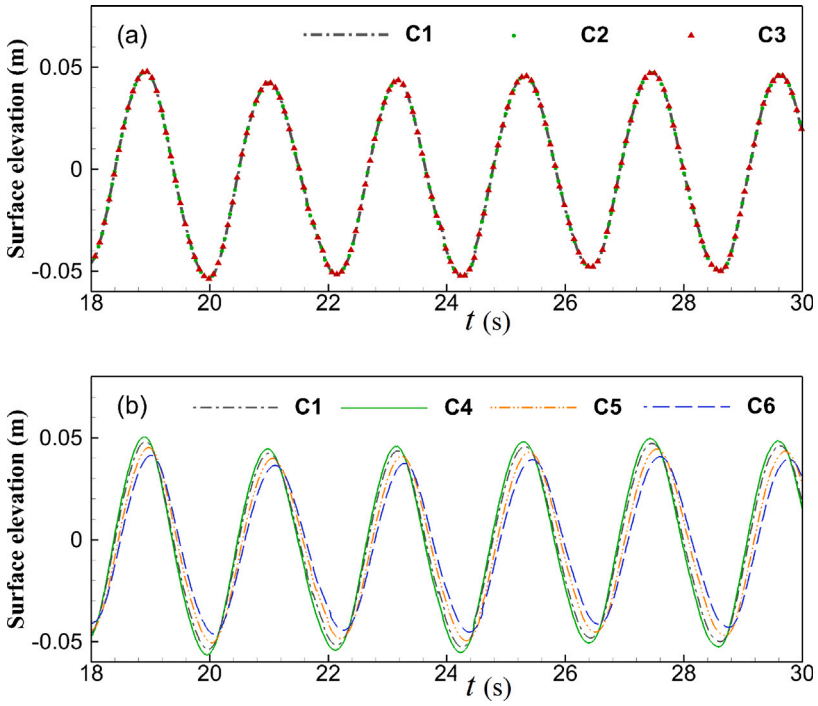

Fig. 5. Time series of surface elevation with different mesh numbers (a) and particle size (b) for case 2.

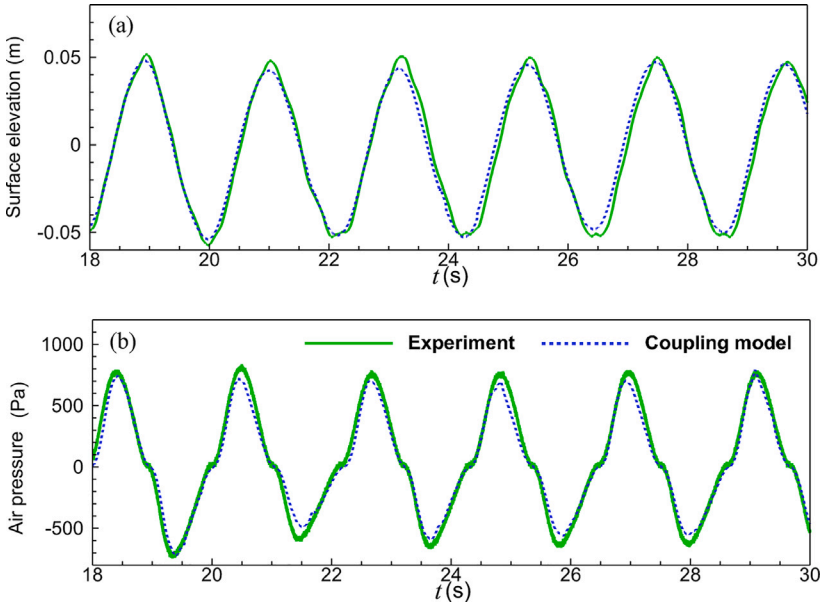

Fig. 6. Time series of surface elevation (a) and air pressure (b) inside the chamber for case 2.

Table 2
Numerical Set up and errors for convergence tests.

Case	Mesh numbers (x, y)	Particle size (m)	MAE_a1	MAE_p1	Cost (h)
C1	1000 × 10	0.01	–	–	15.6
C2	2000 × 10	0.01	0.0%	0.0%	15.7
C3	4000 × 10	0.01	0.0%	0.0%	16.0
C4	1000 × 10	0.005	2.2%	2.8%	64.2
C5	1000 × 10	0.02	2.4%	4.6%	5.7
C6	1000 × 10	0.04	8.8%	9.3%	2.1

numerical simulation is slightly smaller than experimental data for the wave case 2. A mild phase difference can be found for case 2 in the area of positive air pressure. The time series of pressures at pressure sensors for case 2 are shown in Fig. 7. A good agreement between the simulations and the experiments of the wave pressure for case 2 on the inner and outer side of the front wall is achieved as shown in Fig. 7. Fig. 8 shows the variations of the pressure at sensor 3 for all cases. It can be seen that the measured and simulated pressure agree well with each other, although there are some differences between them at the peak pressure. The maximum difference in hydrodynamic efficiency between experimental and numerical simulations is less than 11% as shown in Table 3. As a whole, the numerical model can capture hydrodynamic efficiency and wave loads of the U-OWC breakwater well for the considered wave heights and periods.

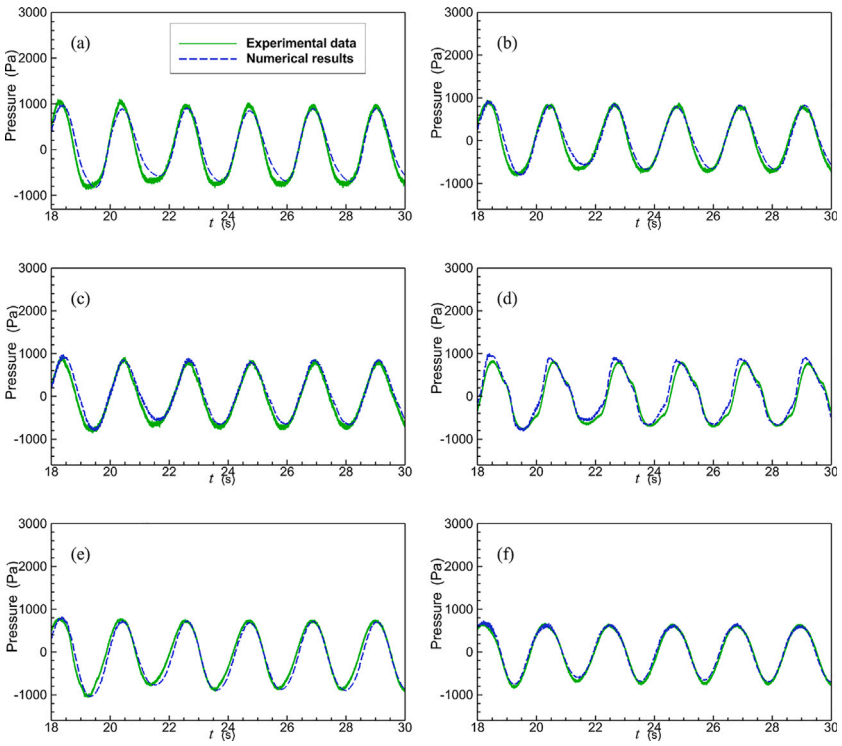

Fig. 7. Time series of pressure at sensor 4 (a), sensor 5 (b), sensor 6 (c), sensor 7 (d), sensor 11 (e), and sensor 12 (f) for case 2.

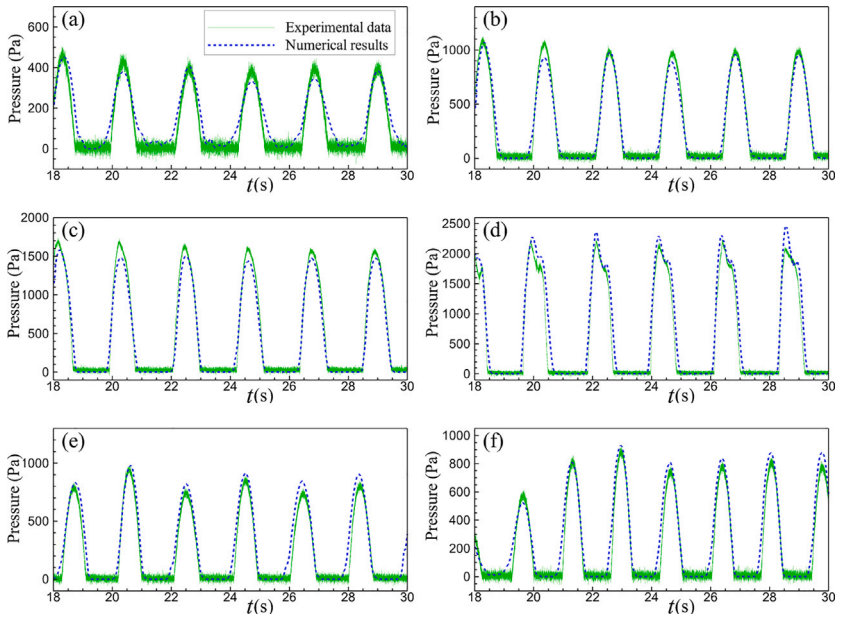

Fig. 8. Time series of pressure at sensor 3 for case 1 (a), case 2 (b), case 3 (c), case 4 (d), case 5 (e), and case 6 (f).

Table 3
Comparisons of hydrodynamic efficiency ξ between experimental and numerical simulations.

	Case 1	Case 2	Case 3	Case 4	Case 5	Case 6
Exp.	0.690	0.543	0.454	0.266	0.415	0.379
Num.	0.721	0.553	0.487	0.284	0.398	0.342
Error (%)	4.5	1.8	7.3	6.3	4.3	10.8

5. Results and discussions

In the above section, the reproducibility of the coupled SPH model for pressure at the measurement point and hydrodynamic efficiency has been verified. For the survivability of U-OWC under rough wave conditions, sliding or overturning failure caused by wave loading need to be considered in the structural design phase. For an U-OWC breakwater, more attention is given to the lip wall in Fig. 9. Wall 2 is completely submerged in water. Therefore, only the forces and the bending moments of wall 1 are discussed, and are shown in Fig. 9. The inflection point 1 of the device is subjected to local maximum

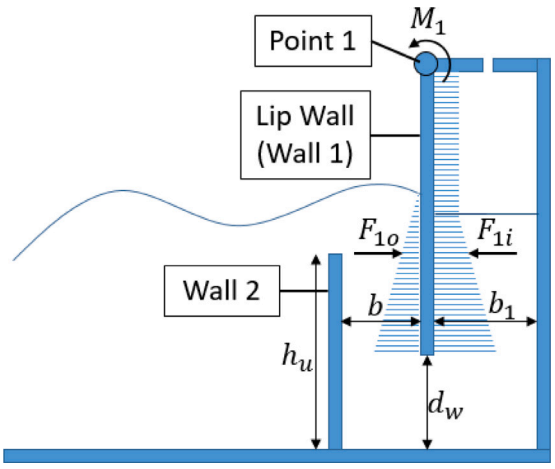

Fig. 9. Schematic of wave force and moment on the U-OWC device.

loads for wall 1, and the point 1 is taken as the rotational centres of wave bending moments. The total horizontal wave force $\mathbf{F_1}$ and wave moment $\mathbf{M_1}$ are the sums of the seaward and shoreward surface components:

$$\mathbf{F_1} = \mathbf{F_{1o}} + \mathbf{F_{1i}} = \sum_j p_j^{out} \Delta x_0 + \sum_j p_j^{in} \Delta x_0, \tag{21}$$

$$\mathbf{M_1} = \sum_j p_j^{out} \Delta x_0 r_{j1} + \sum_j p_j^{in} \Delta x_0 r_{j1}, \tag{22}$$

where $\mathbf{F_{1o}}$ and $\mathbf{F_{1i}}$ denote wave force vector on the wall 1 from outside and inside the chamber, respectively. Positive values of $\mathbf{F_1}$ and $\mathbf{M_1}$ indicate horizontal forces to the right and counterclockwise, respectively. r_1 denotes the distance to the point 1. Δx_0 denotes particle spacing. In this paper, the output frequency of SPH pressure distribution is 100HZ. To avoid the influence of pressure noise on the result observation, Filter function in MATLAB is used to filter the pressure distribution data (the window Size length of the Filter function is 8).

5.1. Effects of wave condition on wave loads

In this subsection, the effect of wave period and height on the horizontal wave forces and wave moments acting on the wall 1 is investigated using the numerical model. Water depth d of 0.675 m, the geometries of chamber, and the damping factor K_{dm} of 1.47 are constant. A range of wave heights and periods are conducted.

5.1.1. Effects of wave height

Firstly, the cases of the incident wave with the same wave period of 2.15 s, and various wave heights (0.05 m, 0.10 m, 0.147 m, 0.198 m, and 0.247 m) are simulated. Fig. 10 shows the time series of horizontal wave forces and wave moments at the lip wall. The symbols for wave forces and moments indicate the direction. As the wave height increases, the time profiles of the wave forces, as well as moments, at the lip wall become more complex. Two local peaks in the positive wave force occur as the wave height increases, $FP1$ and $FP2$, while one local peak in the negative wave force occurs as the wave height increases, called $FP3$. The moments also show two local peaks $MP1$ and $MP2$. The frequency is not affected by wave height. As the wave height is larger, there exist some small oscillations in the variation of wave loads in Figs. 9 10 This is due to the fact that as the wave height increases, the pressure acoustic disturbance also becomes more severe.

As the wave height increases, the two components of the horizontal wave force also gradually increase as shown in Fig. 11. Fig. 12 shows an instantaneous screenshot of the three peak pressures at a wave height of 0.20 m. The air pressure in the chamber is lower than the atmospheric pressure, resulting in a larger positive wave force. Therefore, $FP1$ occurs mainly due to the low air pressure. The part inside the chamber of the lip wall that is exposed to air is closer to point 1. This explains why the moment does not show a local peak while $FP1$ occurs in Fig. 11. F_{1i} and F_{1o} are around their lowest values when $FP1$ occurs as HM1 in Fig. 13. The forces acting on the inner and outer surfaces of the lip wall (F_{1i} and F_{1o}) not only involve the dynamic wave forces but also incorporate the hydrostatic forces, making their average positions over zero as shown in Fig. 13. After $FP1$ occurs, F_{1i} continues to increase and F_{1o} remains at its lowest value for a while (as $HM2$ in Fig. 13). This explains the locally low values of $F1$ between $FP1$ and $FP2$. Then F_{1o} becomes larger gradually. As a result, $F1$ gradually increases with a local peak $FP2$. $FP2$ occurs when F_{1i} is near its initial value. In the model, a quadratic expression is used to represent the relationship between the air flow rate and the air pressure in the chamber. As a result, the air pressure changes more slowly around the zero point as shown in Fig. 13. This variation in air pressure is also reflected in F_{1i}, i.e., pressure growth becomes slow around the initial F_{1i} as $HM3$ in Fig. 13. However F_{out} shows a linear increase i.e., the growth rate of F_{1o} around air pressure zero point is greater than the value of F_{1i}. This is partly responsible for the appearance of the local peak $FP2$. In Fig. 12, the higher free surface of the external water column results in $FP2$ as well as $MP2$. In Fig. 10, $FP3$ with wave force direction pointing out of the chamber occurs when the internal air pressure is greater than the atmospheric pressure. Although the free surface levels are similar on both sides of the lip wall in Fig. 12, the air pressure inside the chamber affects the water pressure and results in local peaks $FP3$ as well as $MP2$.

5.1.2. Effects of wave period

The cases of the incident wave with wave height of 0.20 m, and a range of wave periods (1.75 s, 1.95 s, 2.15 s, 2.35 s, and 2.55 s) were simulated. Fig. 14 shows the time series of horizontal wave forces and wave moments. The time is nondimensionalized as t/T_w. When the period is less than 1.95 s, $FP1$ decreases as the period increases. When the period is greater than 1.95 s, $FP1$ increases with increasing wave period, and $FP2$ decreases with increasing wave period. $FP3$ has a minimum value at a period of 2.15 s, and a maximum value at 2.55 s. The moment $MP1$ decreases with increasing period. $MP2$ decreases as the period increases when the period is less than 2.15 s, and when the period is greater than 2.15 s, $MP2$ increases as the period increases. Also, the value of $MP2$ is greater than $MP1$ when the wave period is greater than 2.35 s. Variations in wave period lead to changes of wave forces on both sides of wall 1 in terms of both amplitude and phase as illustrated in Fig. 15. The phase change also leads to a change in the total wave force and the moment. For example, $FP2$ becomes smaller due to slight phase difference between F_{1i} and F_{1o} for $T_w = 2.55$ s. The above results show that the period of the different incident waves leads to variations in the local peaks. This causes the maximum wave loads to occur at different peaks.

5.2. Effect of geometry parameters on wave loads

As mentioned in previous sections, the U-OWC system investigated here is composed of a submerged wall (Wall 2) in the front of the chamber. The hydrodynamic properties of the U-OWC vary with both the change of the position as well as the change of height of the wall 2. The vertical duct width b and duct height h_u are introduced to represent better the variation of the shape as shown in Fig. 9. Hereinafter, the influences of two geometry parameters: the duct width and the duct height, on wave forces acting on the wall 1 are investigated. When the influence of one of these factors is investigated, the other parameters are kept constant. Simulations are performed for a constant wave height of 0.20 m, a damping factor of $K_{dm} = 1.47$ and ten incident wave periods T_w varied evenly from 1.75 s to 2.65 s.

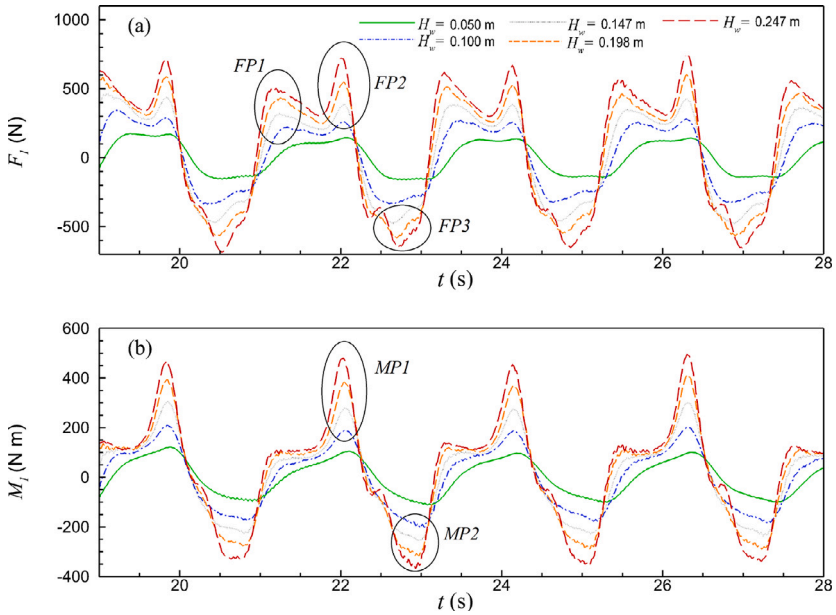

Fig. 10. Numerical time histories of the horizontal wave forces F_1 (a) and wave moments M_1 (b) at lip wall for different wave heights.

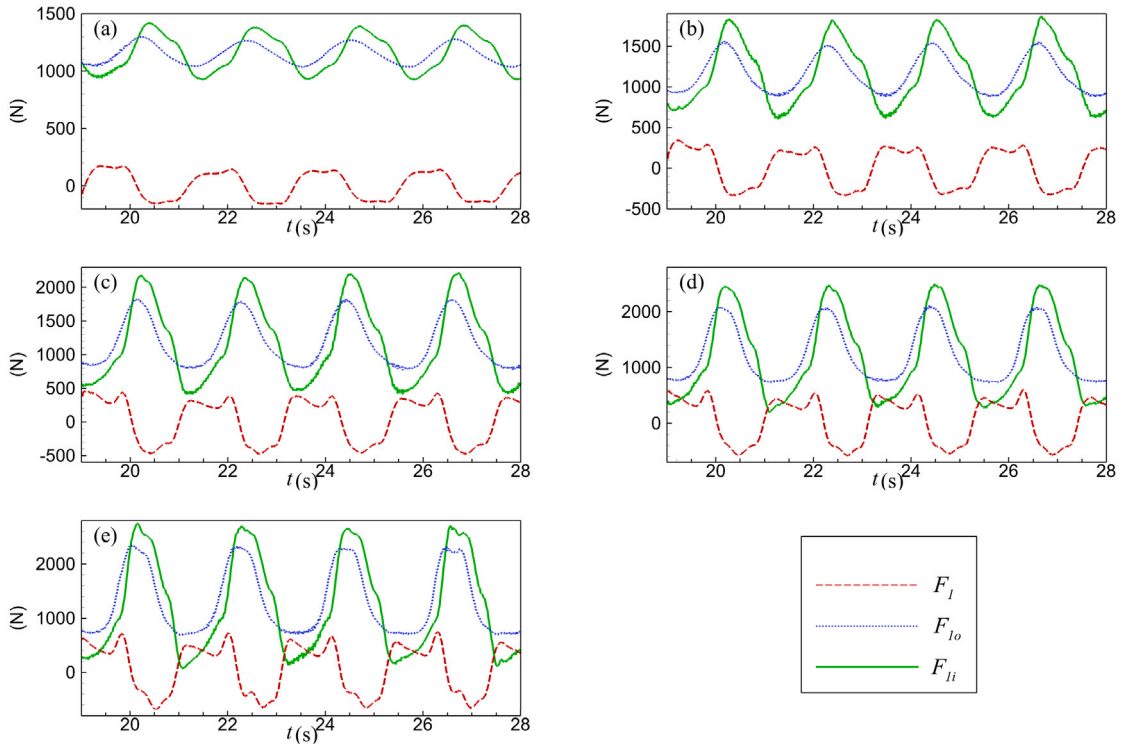

Fig. 11. Numerical time histories of the horizontal wave forces F_1, wave forces on the outer F_{1o} and inner F_{1i} side of the wall 1 for wave height H_w = 0.05 m (a), 0.10 m (b), 0.15 m (c), 0.20 m (d), and 0.25 m (e).

5.2.1. Effects of vertical duct width b/b_1

To investigate the effects of the variation of vertical duct width b on wave load, five different cases are considered, i.e., b = 0.063 m, 0.103 m, 0.143 m, 0.183 m, and 0.223 m. The corresponding relative vertical duct width are b/b_1 = 0.220, 0.360, 0.5, 0.640, and 0.78, where b_1 = 0.286 m is the width of the chamber. The horizontal force peak F_1^{max} and wave moment peak M_1^{max} for the lip wall are shown in Fig. 16. The minimum F_1^{max} for wall 1 is achieved when b/b_1 = 0.5 for wave periods from 1.75 s to 2.25 s. When T_w is greater than 2.35 s, F_1^{max} for wall 1 decreases as b increases. When T_w is less than 2.25 s, the minimum value of M_1^{max} for wall 1 occurs at b/b_1 = 0.5. When T_w is greater than 2.45 s, the minimum M_1^{max} for wall 1 occurs at b/b_1 = 0.78. When b/b_1 = 0.22, the M_1^{max} for wall 1 is maximal for all wave conditions. In general, when T_w is less than 2.25 s, b/b_1 = 0.5 should be chosen from the perspective of reliability. When T_w is larger than 2.45 s, variations of minimum wave force and moment with b/b_1 show an opposite trend.

Fig. 17 shows the variation of hydrodynamic efficiency C_w for five vertical duct widths. When b/b_1 = 0.2, C_w is the lowest for all wave conditions. As b/b_1 increases, the capture efficiency becomes

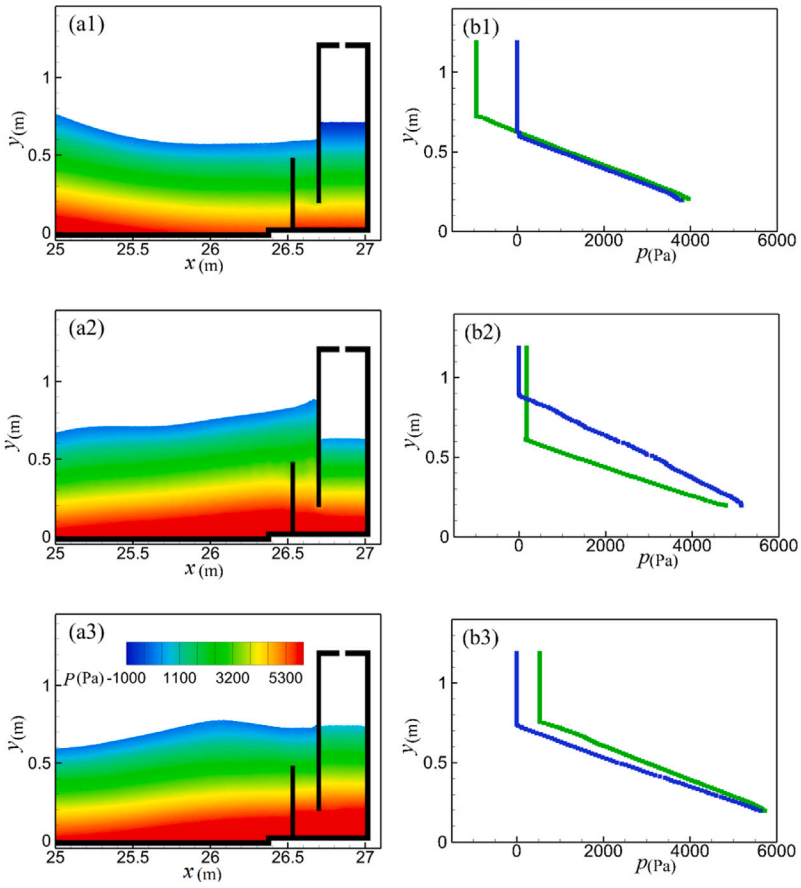

Fig. 12. Numerical pressure field (a) and distribution (b) (blue dots: outer; green dots: inner) on both sides of wall 1 for wave height 0.20 m and wave period 2.15 s at t = 23.2 s (1), 24.1 s (2), and 24.7 s (3). (For interpretation of the references to colour in this figure legend, the reader is referred to the web version of this article.)

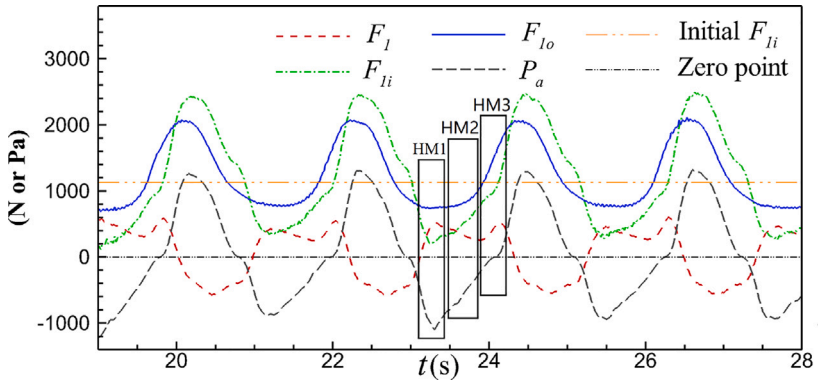

Fig. 13. Numerical time histories of the horizontal wave forces F_1, air pressure p_a inside the chamber, wave forces on the outer F_{1o} and inner F_{1i} side of the wall 1 for wave height H_w = 0.20 m.

greater. In addition, b/b_1 has less effect on the C_w for waves with large periods. Fig. 18 shows the time series of air pressure inside the chamber. Air pressure of the vertical duct widths b/b_1 = 0.2 is less than other widths. This is because the small U-shaped opening width simply causes a smaller oscillation of the water phase inside the chamber. According to Eq. (6), a slower change in air volume results in lower air pressure. Moreover, the C_w highly depends on the air pressure inside the chamber.

Fig. 18 also shows the time histories of the wave forces of the inner and outer side of wall 1 for wave periods of 1.75 s. The variation in air pressure from the width b/b_1 affects the pressure on the inner wall of wall 1. At the same time, the pressure on the outer wall of wall 1 also has some slight influence. In addition, the phase of the peak of the pressure changes. When T_w = 1.75 s, the first force peak $FP1$ is not obvious for b/b_1 = 0.2. As mentioned above, the air pressure affects the first force peak $FP1$. Therefore, $FP1$ is not significant when b/b_1 = 0.2. In fact, F_1^{max} occurs at $FP2$ for all b/b_1 less than 0.5. When b/b_1 is greater than 0.5, F_1^{max} then occurs at $FP1$.

The above analysis shows that a smaller b/b_1 not only reduces the capture ratio but also increases the wave loading, for smaller incident wave periods. When the incident wave period is larger, a smaller b/b_1 leads to smaller efficiency and larger wave moment peaks, but can lead to smaller wave load peaks. Overall, it is not recommended that the submerged front wall be too close to the cavity. This is because it reduces the capture efficiency, and can lead to larger wave loads at some wave conditions as might be expected.

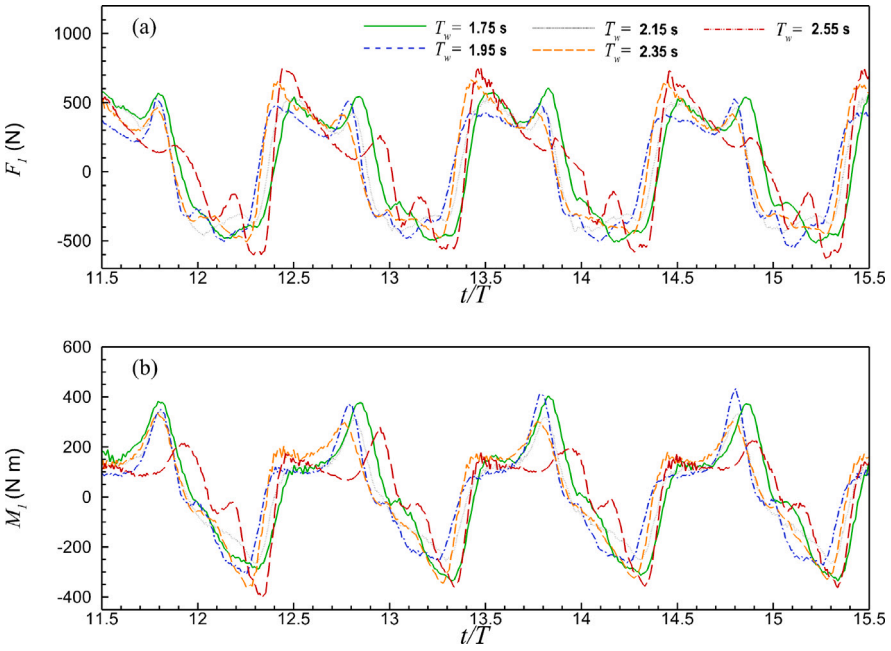

Fig. 14. Numerical time histories of the horizontal wave forces F_1 (a) and wave moments M_1 (b) at wall 1 for different wave periods.

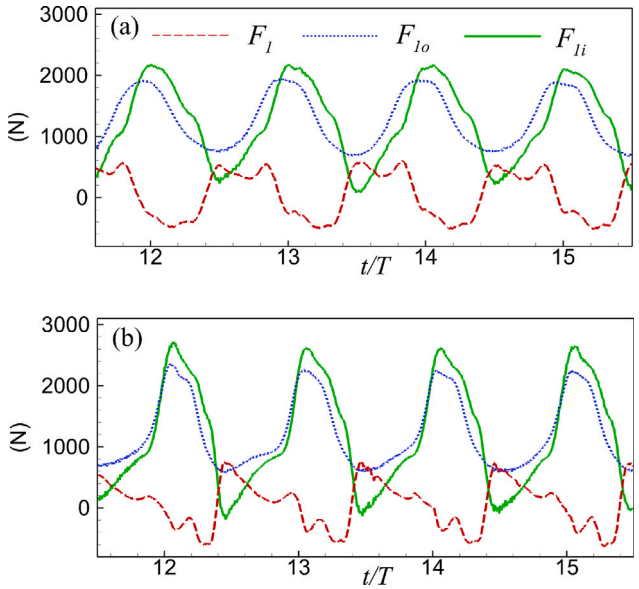

Fig. 15. Numerical time histories of the horizontal wave forces F_1, wave forces on the outer F_{1o} and inner F_{1i} side of the wall 1 for wave period T_w = 1.75 s (a) and 2.55 s (b).

5.2.2. *Effects of vertical duct height h_u/d_w*

To investigate the effects of the variation of vertical duct height h_u on wave load, five different cases are considered, i.e., h_u = 0.079 m, 0.179 m, 0.279 m, 0.379 m, and 0.479 m. The corresponding relative vertical duct heights are h_u/d_w = 0.50, 1.12, 1.74, 2.36 and 2.98, where d_w = 0.164 m is distance between the bottom of the lip wall and the seabed (see Fig. 9). Fig. 19 shows the maximum horizontal force F_1^{max} and wave moment M_1^{max} for the middle duct width b = 0.143 m.

When the wave period T_w is 1.75 s, F_1^{max} for the relative vertical duct height h_u/d_w = 2.36 is lowest for different vertical duct heights. While F_1^{max} for h_u/d_w = 1.74 is smallest for wave periods from 1.75 s to 2.15 s. When T_w is greater than 2.25 s, F_1^{max} decreases as the vertical duct height h_u increases. When T_w is less than 2.05 s, the minimum value of M_1^{max} for wall 1 occurs at h_u/d_w = 2.36. When T_w is greater than 2.15 s, M_1^{max} increases as the vertical duct height h_u increases. When T_w is larger than 2.45 s, the vertical duct height has little impact on the maximum wave moment for wall 1.

Fig. 20 shows the time history of the wave force as well as the moment for wall 1 when wave periods are 1.75 s and 2.55 s. When T_w = 1.75 s, $FP1$ decreases as h_u/d_w increases. However $FP2$ increases as h_u/d_w increases. When h_u/d_w is less than 1.74, F_1^{max} occurs at $FP1$. However F_1^{max} occurs at $FP2$ when h_u/d_w is greater than 2.36. For T_w = 2.55 s, F_1^{max} occurs at $FP1$ when h_u/d_w is less than 2.36. However F_1^{max} occurs at $FP3$ when h_u/d_w = 2.98. When T_w = 1.75 s, the first moment peak $MP1$ increases as the vertical duct height h_u increases. While M_1^{max} occurs at $MP2$ when h_u/d_w = 0.50. M_1^{max} occurs at $MP2$ when h_u/d_w is greater than 1.12. When T_w = 1.75 s, M_1^{max} occurs at $MP2$, and is much less affected by vertical duct height. It can be noticed that the change in h_u/d_w causes F_1^{max} and M_1^{max} to occur at different position of peaks. Therefore, the pattern of maximum load variation may be different for different incident wave periods. Fig. 21 shows the time series of air pressure, wave forces on the inner and outer sides of the wall 1. The change in geometry affects the phase difference between the inner and outer walls. This results in a change in the total horizontal wave force on wall 1 (as shown in Fig. 20).

Fig. 22 shows the variation of hydrodynamic efficiency C_w for five vertical duct heights. When T_w is less than 2.2 s, C_w is the lowest for h_u/d_w = 1.12. When T_w is larger than 2.2 s, C_w is the lowest for h_u/d_w = 1.74. C_w is maximum for all wave conditions when h_u/d_w = 2.98. Finally, the relative vertical duct height h_u/d_w can be larger than 2.36 to achieve relatively larger C_w, small forces and moments for T_w less than 2.2 s. As shown in Fig. 20, the value of F_1^{max} and M_1^{max} exhibit an opposite tendency with the increasing h_u/d_w when T_w greater than 2.2 s. However, the change of F_1^{max} between h_u/d_w = 0.50 and 2.981 is 26% for T_w = 2.65 s. While the change of M_1^{max} is only 6% in the same condition. Meanwhile, the higher h_u/d_w, the greater C_w when h_u/d_w > 1.74. Thus, the height of wall 1 should be higher for large wave periods.

From the numerical simulations in Figs. 17 and 22, the natural period is found to be in the range of approximately 2.2 s. In order to make the conclusions general, several specific wave periods above are reformulated in the conclusions section based on the natural period.

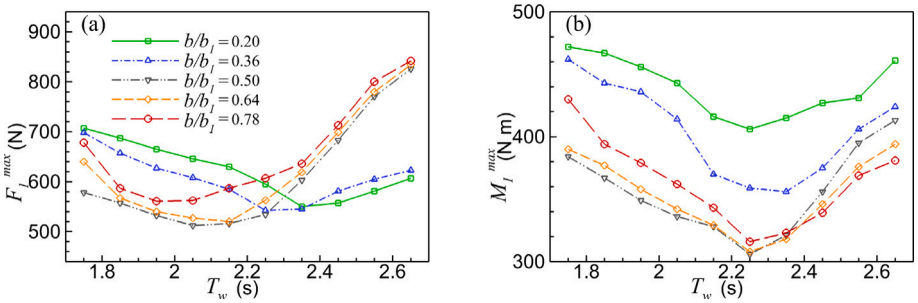

Fig. 16. Numerical horizontal forces peak F_1^{max} and wave moments peak M_1^{max} for different vertical duct widths.

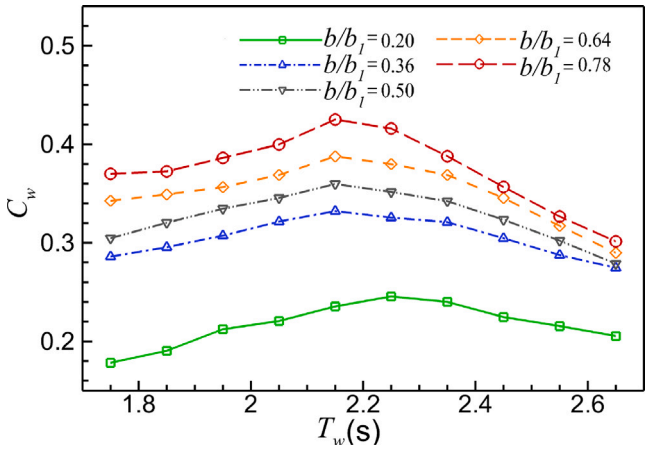

Fig. 17. The comparison of numerical hydrodynamic efficiency C_w for different vertical duct widths.

6. Conclusions

In this work, the coupled SPH model is applied to optimize the U-OWC breakwater. First, the experiments as well as the numerical setup are briefly described. Numerical simulations are performed to assess dependence on the U-OWC geometry. The numerical free surface level in the chamber, the air pressure and the pressure measurement points are compared with the experimental data. The results showed that the model can reproduce the loading and hydrodynamic efficiency of the U-OWC breakwater in a regular wave well. Then, the wave forces and bending moments acting on the lip wall for various wave heights and periods are discussed. Wave force and moments increase with increasing wave height. Three local horizontal force peaks ($FP1$, $FP2$, and $FP3$) and two local moment peaks ($MP1$ and $MP2$) on the lip wall are observed. Changes in wave period lead to changes in the phase difference of force evolution between the inside and outside of the lip wall. As the period changes, the maximum wave load (torque) occurs at one of $FP1$, $FP2$ and $FP3$ ($MP1$ and $MP2$). As a result, the maximum loads show different patterns at different incident wave periods.

The effects of the vertical duct width b and height h_u of U-shaped geometry on the wave force and hydrodynamic efficiency are investigated. When incident wave period is less than the resonant period, the vertical duct width b/b_1 larger than 0.78 leads to a relatively larger capture ratio, smaller horizontal wave force and moment for lip wall. When incident is larger than the resonant period, the maximum horizontal wave forces resulting from optimization of geometry have an opposite trend of change to the maximum wave moment. The maximum horizontal force increases with increasing b/b_1, and maximum moments decrease with increasing b/b_1. When incident wave period is less than the resonant period, the vertical height h_u/d_w larger than 2.36 gives a relatively larger capture ratio, small horizontal wave force and moment for lip wall. When incident wave period is greater than the resonant period, h_u/d_w has a greater effect on maximum horizontal wave forces than maximum bending moments. Hydrodynamic efficiency is only concerned with the air pressure inside the chamber. While the wave load of the lip wall is affected by the phase difference and the air pressure. Therefore, the geometric coefficients have different effects on hydrodynamic efficiency and wave loads.

By optimizing the U-shaped geometry, the maximum wave force and moment can be reduced, and the hydrodynamic efficiency can be improved significantly. The optimum capture efficiency design also has the potential to result in the U-OWC unit being subjected to large wave loads. It is difficult to give an optimum design that satisfies both maximum efficiency and minimum load. Therefore, it is necessary to consider both capture efficiency and wave loads when initially designing an U-OWC breakwater. The above conclusions are restricted to the wave conditions studied in this paper. In the future, more wave conditions will need to be discussed. Moreover, the influence between the individual geometric factors (including the radius of the orifice) needs to be considered.

CRediT authorship contribution statement

Guixun Zhu: Conceptualization, Methodology, Formal analysis, Validation, Writing – original draft, Writing – review & editing. **John Samuel:** Data curation, Writing – review & editing. **Siming Zheng:** Conceptualization, Writing – review & editing, Supervision. **Jason Hughes:** Methodology, Writing – review & editing, Supervision. **David Simmonds:** Writing – review & editing. **Deborah Greaves:** Conceptualization, Writing – review & editing, Supervision.

Declaration of competing interest

The authors declare that they have no known competing financial interests or personal relationships that could have appeared to influence the work reported in this paper.

Data availability

Data will be made available on request.

Acknowledgements

Guixun Zhu was supported by the financial support from China Scholarship Council (Grant No. 201806060137). Siming Zheng acknowledges support from the Open Research Fund Program of the State Key Laboratory of Hydraulic Engineering Simulation and Safety (Tianjin University) [Grant No. HESS-1902]. Deborah Greaves would like to acknowledge the financial support of EPSRC funded Supergen ORE Hub (EP/S000747/1). John Samuel and David Simmonds would like to acknowledge the financial support from PORTOS (Ports Towards Energy Self-Sufficiency), EU project (EAPA 784/2018) that is co-financed by the Interreg Atlantic Area Program through the European Regional Development Fund. John Samuel also would like to acknowledge the financial support from the Supergen Early Career Researcher Research Fund.

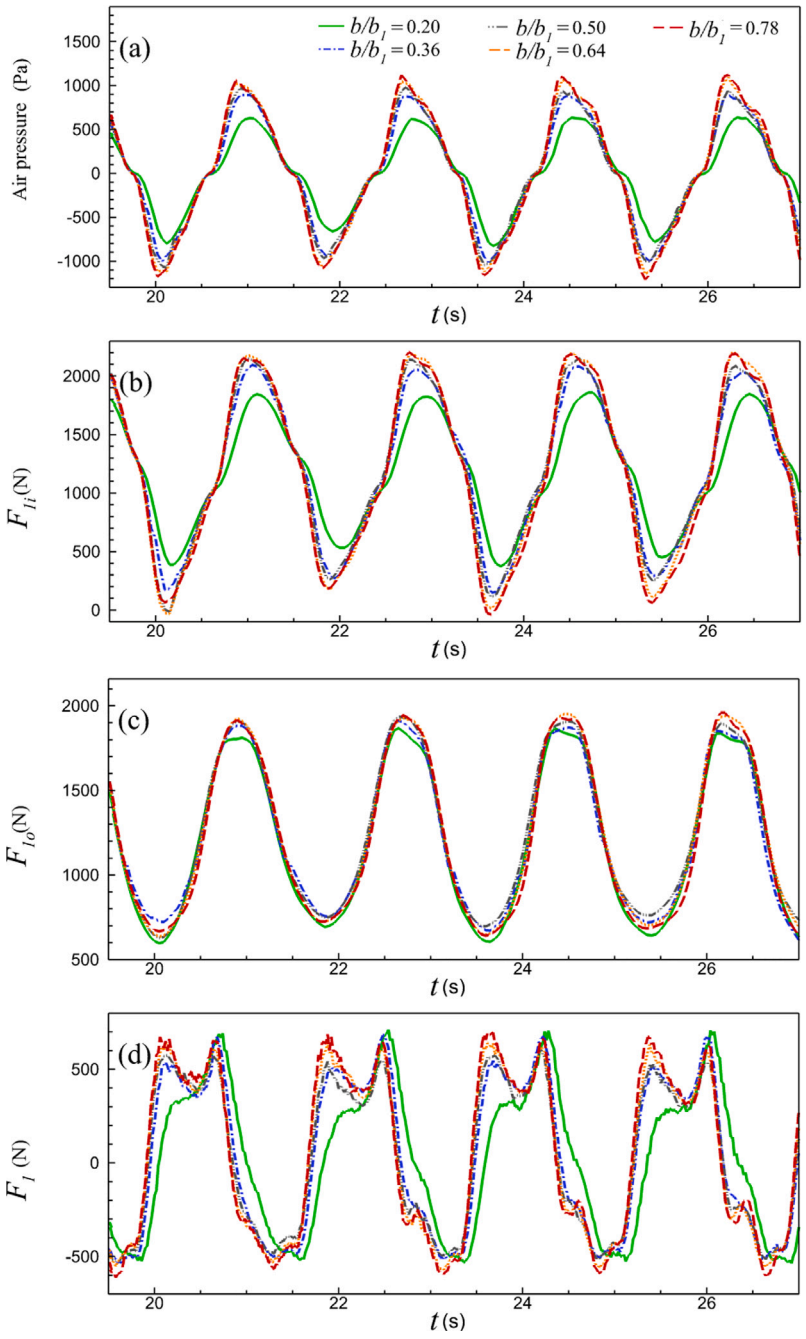

Fig. 18. The comparison of air pressure (a) inside the chamber, wave forces on the inner F_{1o} (b), outer F_{1i} (c) side and the horizontal wave forces F_1 (d) for different vertical duct widths for wave periods $T_w = 1.75$ s.

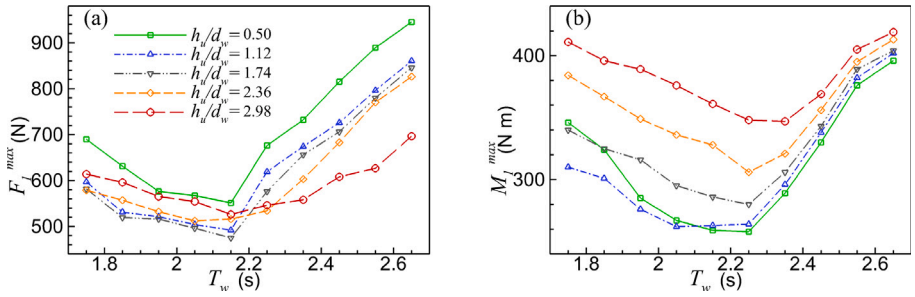

Fig. 19. Numerical maximum horizontal forces F_1^{max} and wave moments M_1^{max} for different vertical duct heights.

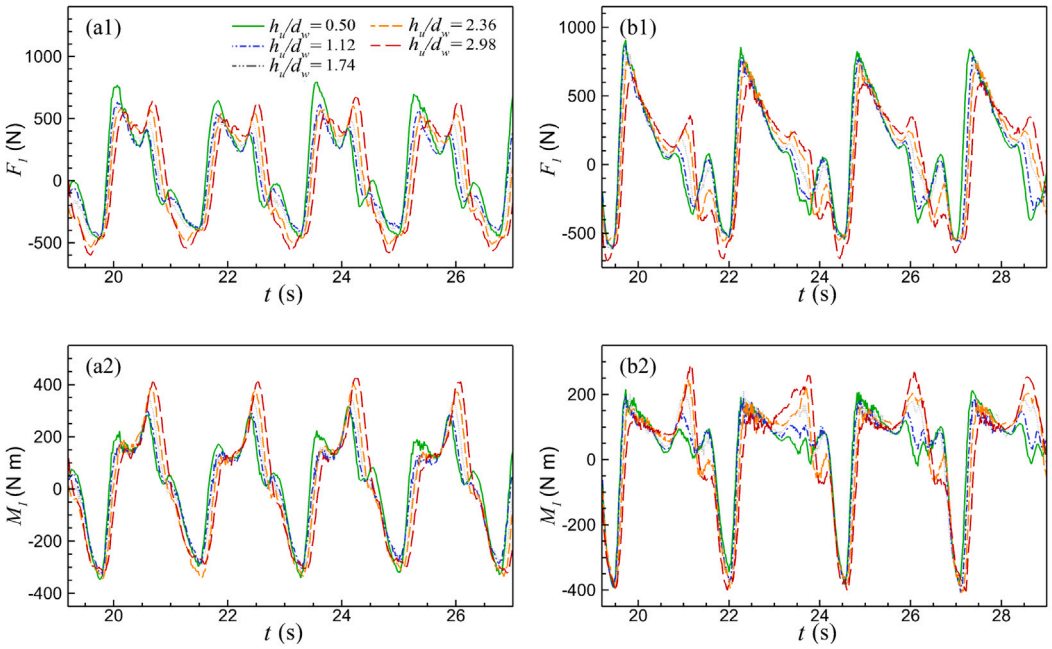

Fig. 20. Numerical time history of wave forces F_1 (1) and wave moments M_1 (2) of wall 1 for wave periods $T_w = 1.75$ s (a) and $T_w = 2.55$ s (b).

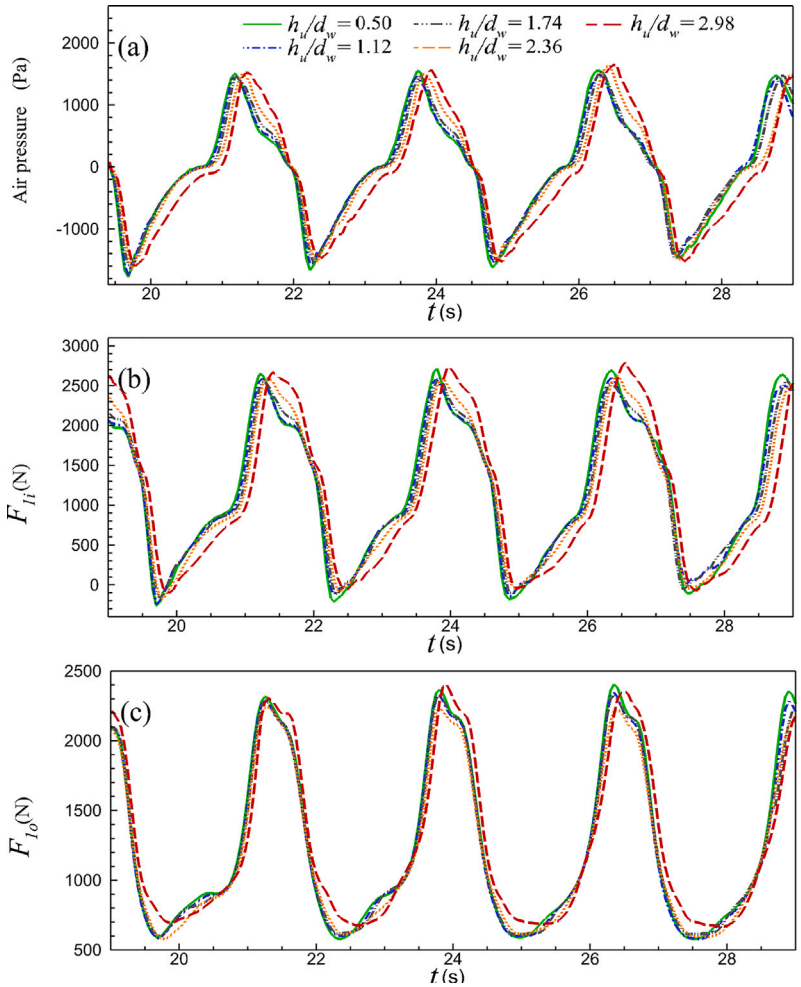

Fig. 21. The comparison of air pressure (a) inside the chamber, wave forces on the inner F_{1o} (b) and outer F_{1i} (c) side for different vertical duct widths for wave periods $T_w = 2.55$ s.

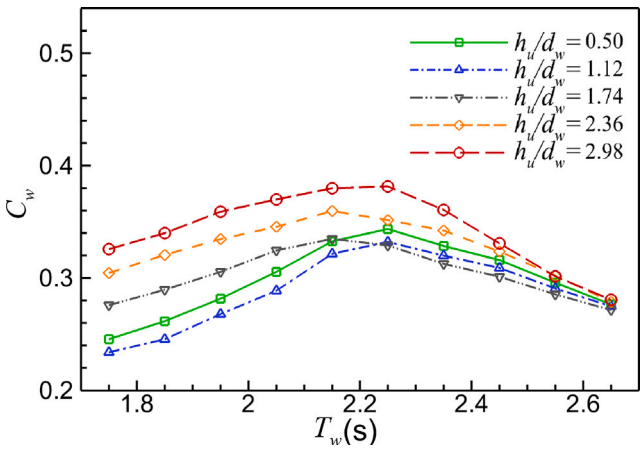

Fig. 22. The comparison of hydrodynamic efficiency C_w for different vertical duct heights.

References

[1] Falcão AFO, Henriques JCC. Oscillating water column wave energy converters and air turbines: A review. Renew Energy 2016;85:1391–424.
[2] Evans DV. The oscillating water column wave energy device. IMA J Appl Math 1978;22(4):423–33.
[3] Evans DV. Wave-power absorption by systems of oscillating surface pressure distributions. J Fluid Mech 1982;114:481–99.
[4] Sarmento AJNA, Falcão AFO. Wave generation by an oscillating surface-pressure and its application in wave-energy extraction. J Fluid Mech 1985;150:467–85.
[5] Evans DV, Porter R. Hydrodynamic characteristics of an oscillating water column device. Appl Ocean Res 1995;17(3):155–64.
[6] Ning DZ, Shi J, Zou QP, Teng B. Investigation of hydrodynamic performance of an OWC (oscillating water column) wave energy device using a fully nonlinear HOBEM (higher-order boundary element method). Energy 2015;83:177–88.
[7] Wang RW, Ning DZ, Zhang CW, Zou QP, Liu Z. Nonlinear and viscous effects on the hydrodynamic performance of a fixed OWC wave energy converter. Coast Eng 2018;131:42–50.
[8] El Marjani A, Ruiz FC, Rodriguez M, Santos MP. Numerical modelling in wave energy conversion systems. Energy 2008;33(8):1246–53.
[9] Zhang Y, Zou QP, Greaves D. Air–water two-phase flow modelling of hydrodynamic performance of an oscillating water column device. Renew Energy 2012;41:159–70.
[10] Luo Y, Wang Z, Peng G, Xiao Y, Zhai L, Liu X, et al. Numerical simulation of a heave-only floating OWC (oscillating water column) device. Energy 2014;76:799–806.
[11] Kamath A, Bihs H, Arntsen ØA. Numerical investigations of the hydrodynamics of an oscillating water column device. Ocean Eng 2015;102:40–50.
[12] Iturrioz A, Guanche R, Lara JL, Vidal C, Losada IJ. Validation of OpenFOAM® for oscillating water column three-dimensional modeling. Ocean Eng 2015;107:222–36.
[13] Vyzikas T, Deshoulières S, Giroux O, Barton M, Greaves D. Numerical study of fixed Oscillating Water Column with RANS–type two–phase CFD model. Renew Energy 2017;102:294–305.
[14] Simonetti I, Cappietti L, Elsafti H, Oumeraci H. Optimization of the geometry and the turbine induced damping for fixed detached and asymmetric OWC devices: A numerical study. Energy 2017;139:1197–209.
[15] Simonetti I, Cappietti L, Elsafti H, Oumeraci H. Evaluation of air compressibility effects on the performance of fixed OWC wave energy converters using CFD modelling. Renew Energy 2018;119:741–53.
[16] Deng Z, Wang C, Wang P, Higuera P, Wang R. Hydrodynamic performance of an offshore-stationary OWC device with a horizontal bottom plate: Experimental and numerical study. Energy 2019;187:115941.
[17] López I, Carballo R, Taveira-Pinto F, Iglesias G. Sensitivity of OWC performance to air compressibility. Renew Energy 2020;145:1334–47.
[18] Wang C, Zhang Y. Numerical investigation on the wave power extraction for a 3D dual-chamber oscillating water column system composed of two closely connected circular sub-units. Appl Energy 2021;295:117009.
[19] Patterson C, Dunsire R, Hillier S. Development of wave energy breakwater at Siadar, Isle of Lewis. In: Coasts, marine structures and breakwaters: adapting to change: proceedings of the 9th international conference organised by the institution of civil engineers and held in Edinburgh on 16 to 18 September 2009. Thomas Telford Ltd; 2010, p. 738–49.
[20] Boccotti P. Design of breakwater for conversion of wave energy into electrical energy. Ocean Eng 2012;51:106–18.
[21] Kuo YS, Lin CS, Chung CY, Wang YK. Wave loading distribution of oscillating water column caisson breakwaters under non-breaking wave forces. J Mar Sci Technol 2015;23(1):10.
[22] John Ashlin S, Sannasiraj SA, Sundar V. Wave forces on an oscillating water column device. Procedia Eng 2015;116:1019–26.
[23] Ning DZ, Wang RQ, Gou Y, Zhao M, Teng B. Numerical and experimental investigation of wave dynamics on a land-fixed OWC device. Energy 2016;115:326–37.
[24] Konispoliatis DN, Mazarakos TP, Mavrakos SA. Hydrodynamic analysis of three–unit arrays of floating annular oscillating–water–column wave energy converters. Appl Ocean Res 2016;61:42–64.
[25] Viviano A, Naty S, Foti E, Bruce T, Allsop W, Vicinanza D. Large-scale experiments on the behaviour of a generalised oscillating water column under random waves. Renew Energy 2016;99:875–87.
[26] Elhanafi A. Prediction of regular wave loads on a fixed offshore oscillating water column-wave energy converter using CFD. J. Ocean Eng Sci 2016;1(4):268–83.
[27] Elhanafi A, Macfarlane G, Fleming A, Leong Z. Experimental and numerical measurements of wave forces on a 3D offshore stationary OWC wave energy converter. Ocean Eng 2017;144:98–117.
[28] Viviano A, Naty S, Foti E. Scale effects in physical modelling of a generalized OWC. Ocean Eng 2018;162:248–58.
[29] Huang Z, Xu C, Huang S. A CFD simulation of wave loads on a pile-type oscillating-water-column device. J Hydrodyn 2019;31(1):41–9.
[30] Pawitan KA, Dimakopoulos AS, Vicinanza D, Allsop W, Bruce T. A loading model for an OWC caisson based upon large-scale measurements. Coast Eng 2019;145:1–20.
[31] Viviano A, Musumeci RE, Vicinanza D, Foti E. Pressures induced by regular waves on a large scale OWC. Coast Eng 2019;152:103528.
[32] Wang R-Q, Ning D-Z. Dynamic analysis of wave action on an OWC wave energy converter under the influence of viscosity. Renew Energy 2020;150:578–88.
[33] Wang R-Q, Ning D-Z, Zou Q-P. Wave loads on a land-based dual-chamber Oscillating Water Column wave energy device. Coast Eng 2020;160:103744.
[34] Zhou Y, Ning D, Chen L, Zhang C, Lin L, Sulisz W. Nonlinear wave loads on a stationary cylindrical-type oscillating water column wave energy converter. Ocean Eng 2021;236:109481.
[35] Bhattacharyya R, McCormick ME. Wave energy conversion. In: Elsevier ocean engineering book series, vol. 6. Elsevier; 2003, p. 477–562.
[36] Vicinanza D, Lauro ED, Contestabile P, Gisonni C, Lara JL, Losada IJ. Review of innovative harbor breakwaters for wave-energy conversion. J Waterw Port Coast Ocean Eng 2019;145(4):03119001.
[37] Didier E, Neves DRCB, Teixeira PRF, Dias J, Neves MG. Smoothed Particle Hydrodynamics numerical model for modeling an oscillating water chamber. Ocean Eng 2016;123:397–410.
[38] Crespo AJC, Altomare C, Domínguez JM, González-Cao J, Gómez-Gesteira M. Towards simulating floating offshore oscillating water column converters with Smoothed Particle Hydrodynamics. Coast Eng 2017;126:11–26.
[39] Wen H, Ren B, Yu X. An improved SPH model for turbulent hydrodynamics of a 2D oscillating water chamber. Ocean Eng 2018;150:152–66.
[40] Zhu G, Graham D, Zheng S, Hughes J, Greaves D. Hydrodynamics of onshore oscillating water column devices: A numerical study using smoothed particle hydrodynamics. Ocean Eng 2020;218:108226.
[41] Quartier N, Crespo AJC, Domínguez JM, Stratigaki V, Troch P. Efficient response of an onshore Oscillating Water Column Wave Energy Converter using a one-phase SPH model coupled with a multiphysics library. Appl Ocean Res 2021;115:102856.
[42] Boccotti P. On a new wave energy absorber. Ocean Eng 2003;30(9):1191–200.
[43] Boccotti P. Caisson breakwaters embodying an OWC with a small opening—Part I: Theory. Ocean Eng 2007;34(5–6):806–19.
[44] Ning DZ, Guo BM, Wang RQ, Vyzikas T, Greaves D. Geometrical investigation of a U-shaped oscillating water column wave energy device. Appl Ocean Res 2020;97:102105.
[45] Boccotti P, Filianoti P, Fiamma V, Arena F. Caisson breakwaters embodying an OWC with a small opening—Part II: A small-scale field experiment. Ocean Eng 2007;34(5–6):820–41.
[46] Arena F, Romolo A, Malara G, Ascanelli A. On design and building of a U-OWC wave energy converter in the Mediterranean Sea: A case study. In: International Conference on Offshore Mechanics and Arctic Engineering, vol. 55423. American Society of Mechanical Engineers; 2013, p. V008T09A102.
[47] Malara G, Arena F. Analytical modelling of an U-oscillating water column and performance in random waves. Renew Energy 2013;60:116–26.
[48] Malara G, Arena F. Response of U-oscillating water column arrays: Semi-analytical approach and numerical results. Renew Energy 2019;138:1152–65.
[49] Scialò A, Henriques JCC, Malara G, Falcão AFO, Gato LMC, Arena F. Power take-off selection for a fixed U-OWC wave power plant in the Mediterranean Sea: The case of Roccella Jonica. Energy 2021;215:119085.
[50] Scandura P, Malara G, Arena F. The inclusion of nonlinearities in a mathematical model for U-Oscillating Water Column wave energy converters. Energy 2021;218:119320.
[51] Spanos PD, Strati FM, Malara G, Arena F. An approach for nonlinear stochastic analysis of U-shaped OWC wave energy converters. Probab Eng Mech 2018;54:44–52.

[52] Strati FM, Malara G, Laface V, Romolo A, Arena F. A control strategy for PTO systems in a U-OWC device. In: International conference on offshore mechanics and arctic engineering, vol. 56499. American Society of Mechanical Engineers; 2015, p. V003T02A066.
[53] Arena F, Daniele L, Fiamma V, Fontana M, Malara G, Moretti G, et al. Field experiments on dielectric elastomer generators integrated on a U-OWC wave energy converter. In: International Conference on Offshore Mechanics and Arctic Engineering, vol. 51319. American Society of Mechanical Engineers; 2018, p. V010T09A028.
[54] Xu C, Liu Z, Tang G. Experimental study of the hydrodynamic performance of a U-oscillating water column wave energy converter. Ocean Eng 2022;265:112598.
[55] Antuono M, Colagrossi A, Marrone S. Numerical diffusive terms in weakly–compressible SPH schemes. Comput Phys Comm 2012;183(12):2570–80.
[56] Marrone S, Antuono M, Colagrossi A, Colicchio G, Touzé DL, Graziani G. δ–SPH model for simulating violent impact flows. Comput Methods Appl Mech Engrg 2011;200(13):1526–42.
[57] Sun PN, Colagrossi A, Marrone S, Zhang AM. The δplus-SPH model: Simple procedures for a further improvement of the SPH scheme. Comput Methods Appl Mech Engrg 2017;315:25–49.
[58] Zhu G, Hughes J, Zheng S, Greaves D. Investigation of the hydrodynamic performance of an oscillating water column wave energy device using a smoothed particle hydrodynamics model. In: Proceedings of the European wave and tidal energy conference, vol. 2394. 2021, p. 1–5.
[59] Monaghan JJ. On the problem of penetration in particle methods. J Comput Phys 1989;82(1):1–15.
[60] Bouscasse B, Colagrossi A, Marrone S, Antuono M. Nonlinear water wave interaction with floating bodies in SPH. J Fluids Struct 2013;42:112–29.
[61] Bingham HB, Zhang H. On the accuracy of finite-difference solutions for nonlinear water waves. J. Eng. Math. 2007;58(1):211–28.
[62] Engsig-Karup AP, Bingham HB, Lindberg O. An efficient flexible-order model for 3D nonlinear water waves. J Comput Phys 2009;228(6):2100–18.
[63] Currie IG. Fundamental mechanics of fluids. CRC Press; 2016.
[64] Larsen J, Dancy H. Open boundaries in short wave simulations—a new approach. Coast Eng 1983;7(3):285–97.
[65] Mayer S, Garapon A, Sørensen LS. A fractional step method for unsteady free-surface flow with applications to nonlinear wave dynamics. Internat J Numer Methods Fluids 1998;28(2):293–315.
[66] Jacobsen NG, Fuhrman DR, Fredsøe J. A wave generation toolbox for the open-source CFD library: OpenFoam®. Internat J Numer Methods Fluids 2012;70(9):1073–88.
[67] Zhu G, Hughes J, Zheng S, Greaves D. A novel MPI-based parallel smoothed particle hydrodynamics framework with dynamic load balancing for free surface flow. Comput Phys Comm 2023;284:108608.
[68] Zhu G. Towards the development of smoothed particle hydrodynamics model for oscillating water column devices [Ph.D. thesis], University of Plymouth; 2023.
[69] López I, Pereiras B, Castro F, Iglesias G. Optimisation of turbine-induced damping for an OWC wave energy converter using a RANS–VOF numerical model. Appl Energy 2014;127:105–14.
[70] López I, Pereiras B, Castro F, Iglesias G. Holistic performance analysis and turbine-induced damping for an OWC wave energy converter. Renew Energy 2016;85:1155–63.
[71] Wang C, Zhang Y. Hydrodynamic performance of an offshore Oscillating Water Column device mounted over an immersed horizontal plate: A numerical study. Energy 2021;222:119964.